

Electronic Supplementary Material (ESI) for Nanoscale.
This journal is © The Royal Society of Chemistry 2017

Electronic Supplementary Information

Gas molecule sensing of van der Waals tunnel field effect transistors

Hong Kyw Choi, Jaesung Park, Nojoon Myoung, Ho-Jong Kim, Jin Sik Choi, Young Kyu Choi, Chi-Young Hwang, Jin Tae Kim, Serin Park, Yoonsik Yi, Soo Kyung Chang, Hee Chul Park, Chanyong Hwang, Choon-Gi Choi and Young-Jun Yu

1. Comparison and alignment for work function between various 2D crystals.

Since the tunneling behavior of tunneling graphene FETs (t-GFETs) is dominantly confirmed by different electron affinities between graphene and 2D crystals barriers, we compared electron affinities for graphene (4.57 eV), WS₂ (4.5 eV), WSe₂ (4.1 eV), MoS₂ (4.0 eV), MoSe₂ (3.9 eV) and hBN (2.3 eV), as shown in Fig. S1(a).[34-38] As a result, because we find low and high electron affinity differences for WS₂ and for hBN with graphene, respectively, we employed these representative barriers with WS₂ and hBN for t-GFETs. The energy band diagrams for G/WS₂/G and G/hBN/G can be aligned with this initial work function difference, as shown in Fig. S1 (b) and (c).

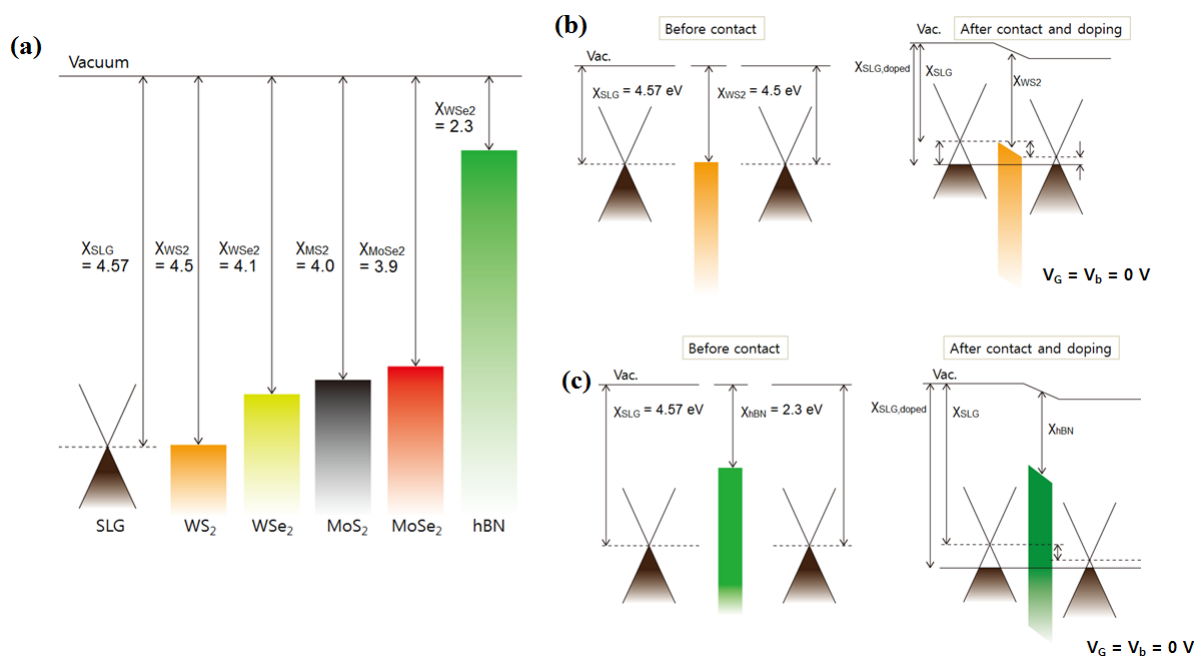
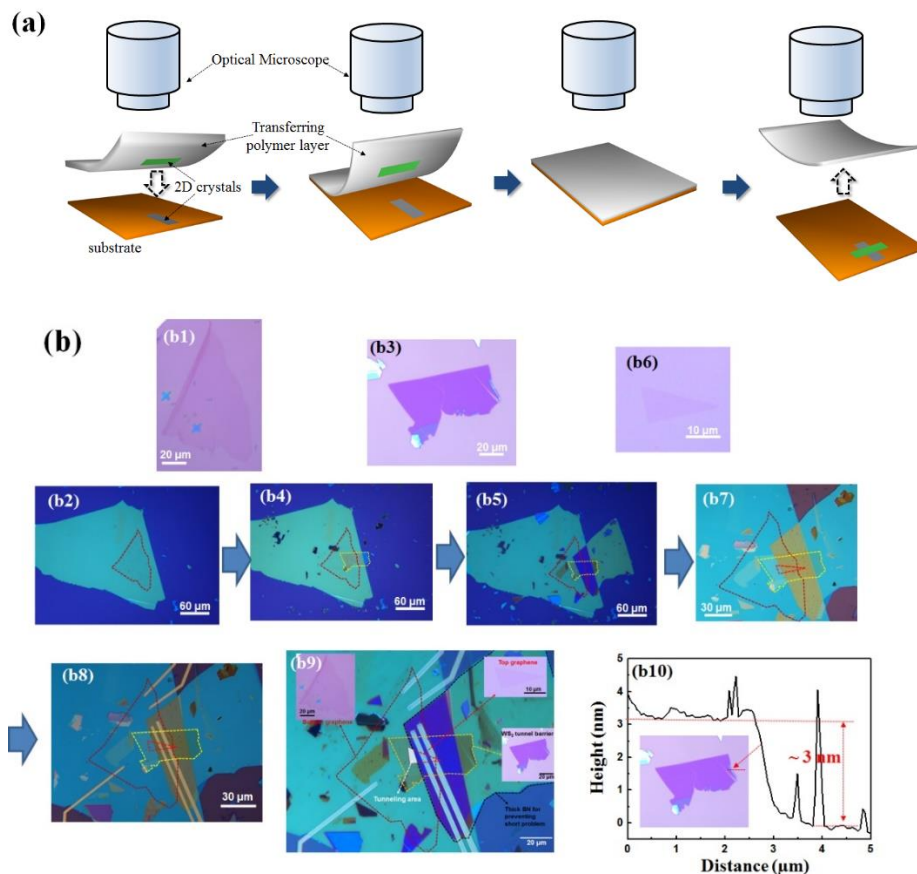


Figure S1. (a) Schematic diagram for a comparison of the electron affinities between 2D crystals of graphene, WS₂, WSe₂, MoS₂, MoSe₂ and hBN. (b) Schematic diagrams of the band alignment between graphene and WS₂ before and after the contact condition. (c) Schematic diagrams of the band alignment between graphene and hBN before and after the contact condition.

2. Fabrication steps for tunneling field-effect transistors based on the van der Waals heterostructure

Van der Waals heterostructures based on single-layer graphene (SLG), WS₂ and hexagonal boron nitride (hBN) are stacked by a normal micrometer manipulation transfer system, as shown in Fig. S2(a). Here, we utilized PMMA as the transferring polymer, and the PMMA was removed by acetone after transferring the 2D crystals. The t-G/WS₂/G and t-G/hBN/G FETs in this work were structured with a top-SLG (T-SLG)/WS₂ or hBN tunnel barrier/bottom-SLG (B-SLG), as shown in Figs. S2(b) and (c), respectively. First, we transferred B-SLG on an hBN layer with an approximate thickness of several hundreds of nanometers onto a 270-nm-thick SiO₂/Si substrate (S2(b2) and S2(c2)). While the B-SLG for t-G/WS₂/G was directly stacked without fabrication (Fig. S2(b4)), the B-SLG for t-G/hBN/G, after transferring B-SLG onto the hBN on SiO₂/Si substrates several hundreds of nm thick, was fabricated for three channels by a normal e-beam lithography process (Fig. S2(c3)). For the tunnel-barrier GFET, thin WS₂ or hBN (2~3 nm thickness) was stacked onto these B-SLG channels (Figs. S2(b5) and 2(c5)). The T-SLG was then stacked onto the WS₂/B-SLG or the hBN/B-SLG layer (Figs. S2(b7) and S2(c7)). Finally, we attached metal electrodes to the T-SLG and B-SLG (Ti/Au= 3 nm/ 80 nm thickness) by a normal e-beam lithography process (Fig. S2(b8) and S2(c8)).



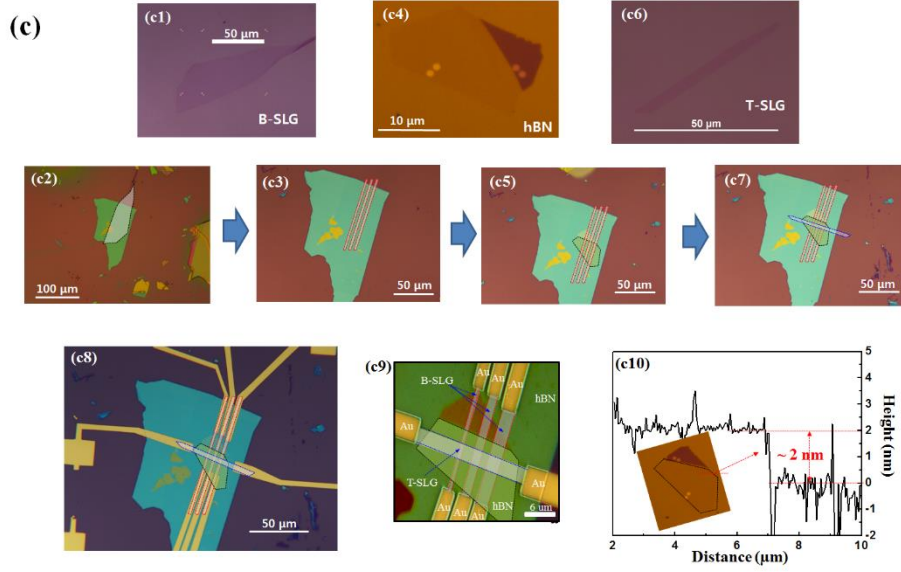


Figure S2. (a) Schematic diagram of the transfer steps used for the vdW heterostructure. Here, we utilized a transferring polymer layer with PMMA. (b) (b1) Optical images of B-SLG on a PMMA substrate. (b2) Optical image of B-SLG transferred onto an hBN substrate approximately several hundreds of nm thick. (b3) Optical image of a thin WS₂ layer (1~2 nm thickness) on a PMMA substrate. (b4) Optical image of thin WS₂ transferred onto a B-SLG/hBN heterostructure. (b5) Optical image of an hBN substrate approximately several hundreds of nm thick partially transferred onto the WS₂/B-SLG/hBN heterostructure to avoid undesired contact between the T-SLG, B-SLG and WS₂ layers. (b6) Optical image of T-SLG on a PMMA substrate. (b7) Optical image of T-SLG transferred onto the WS₂/B-SLG/hBN heterostructure. (b8) Optical image of a T-SLG/WS₂/B-SLG/hBN tunnel FET in contact with Ti/Au metal electrodes. (b9) Optical image of various enlarged T-SLG/WS₂/B-SLG/hBN tunnel FETs. (b10) Height profile of the WS₂ barrier according to AFM measurements. (c) (c1) Optical image of B-SLG on a PMMA substrate. (c2) Optical image of B-SLG transferred onto an hBN substrate approximately several hundreds of nm thick. (c3) Three B-SLG channels fabricated by a normal e-beam lithography process. (c4) Optical image of a thin hBN layer (1~2 nm thickness) on a PMMA substrate. (c5) Optical image of thin hBN transferred onto the B-SLG/hBN heterostructure. (c6) Optical image of T-SLG on a PMMA substrate. (c7) Optical image of T-SLG transferred onto the hBN/B-SLG/hBN heterostructure. (c8) Optical image of a T-SLG/hBN/B-SLG/hBN tunnel FET in contact with Ti/Au metal electrodes. (c9) Optical image of various enlarged T-SLG/hBN/B-SLG/hBN tunnel FETs. (c10) Height profile of the hBN barrier according to AFM measurements.

3. Initial doping condition of T-SLG and B-SLG in t-GFETs

The carrier transport curves as a function of the global gate voltage (V_G) through a highly p-doped Si substrate, as shown in Figs. S3(a), (b) and (c), yield initially the accumulated charge carrier density $n = (C/e)V_{\text{CNP}}$ of the T-SLG ($n_{\text{T-SLG}}$) and B-SLG ($n_{\text{B-SLG}}$) channels in the t-G/WS₂/G and t-G/hBN/G FETs of $n_{\text{T-SLG}} = 1.57 \times 10^{12} \text{ cm}^{-2} \sim 5.24 \times 10^{12} \text{ cm}^{-2}$ ($V_{\text{CNP}} = 30 \text{ V} \sim 100 \text{ V}$) and $n_{\text{B-SLG}} = 0 \sim 1.57 \times 10^{12} \text{ cm}^{-2}$ ($V_{\text{CNP}} = 0 \sim 30 \text{ V}$), respectively. Here, $C = 8.4 \text{ nF/cm}^2$, e and V_{CNP} denote the capacitance with the 270-nm-thick SiO₂ and the 100-nm-thick hBN dielectric layer, the electron charge, and the charge-neutral position of the SLG, respectively. This indicates that highly p-doped T-SLG is influenced more by the humidity and residue in an ambient condition than B-SLG encapsulated by thin and thick h-BN layers. This allows us to confirm, as shown in Fig. S3, that the initial Fermi energy potential differences (ΔE) between T-SLG and B-SLG are (a) ~140 meV, (b) ~120 meV and (c) ~130 meV, as derived with $\Delta E = \hbar \cdot v_F \cdot \pi^{1/2} \cdot [(n_{\text{T-SLG}})^{1/2} - (n_{\text{B-SLG}})^{1/2}]$, where \hbar and $v_F = 1 \times 10^6 \text{ m/s}$ are the Planck constant and the Fermi velocity of SLG, respectively

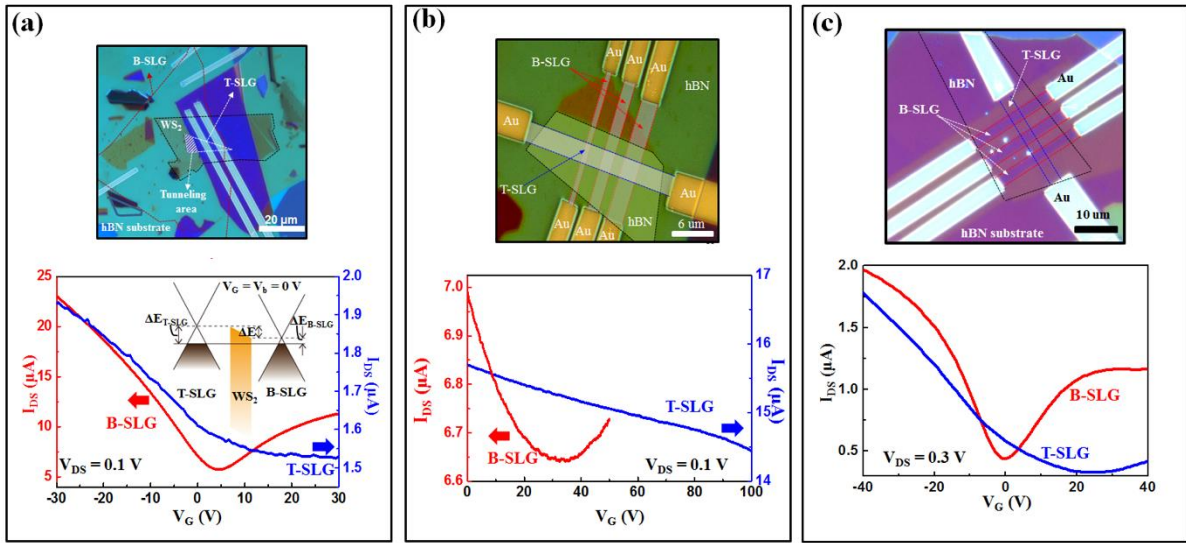


Figure S3. (a)-(b) Optical images and current (I_{DS}) variation of T-SLG and B-SLG as a function of the back gate voltage (V_G) of (a) t-G/WS₂/G and (b), (c) t-G/hBN/G and when applying drain-source voltages (V_{DS}) of 0.1 V and 0.3 V, respectively. Inset of (a): Energetic diagrams of t-G/WS₂/G with $V_G = V_b = 0$ V, where ΔE is the Fermi energy difference between T-SLG and B-SLG.

4. Gas-molecule-sensing sensitivity comparison between a SLG FET and t-GFET

As shown in Fig. S4(a), we measured the current variation ($\Delta I/I_0$) for a T-SLG FET and the relative tunneling current variation ($\Delta I_t/I_0$) for a t-G/hBN/G FET as a function of time (0 ~ 400 s) under exposure to NO₂ gas (30 ppm). As a result, we observed higher sensitivity for the tunnel FET structure as compared to a bare graphene channel, as presented in Fig. S4(b). Thus, if there is a suitable combination between tunneling the channels and the barrier, the sensitivity can be enhanced.

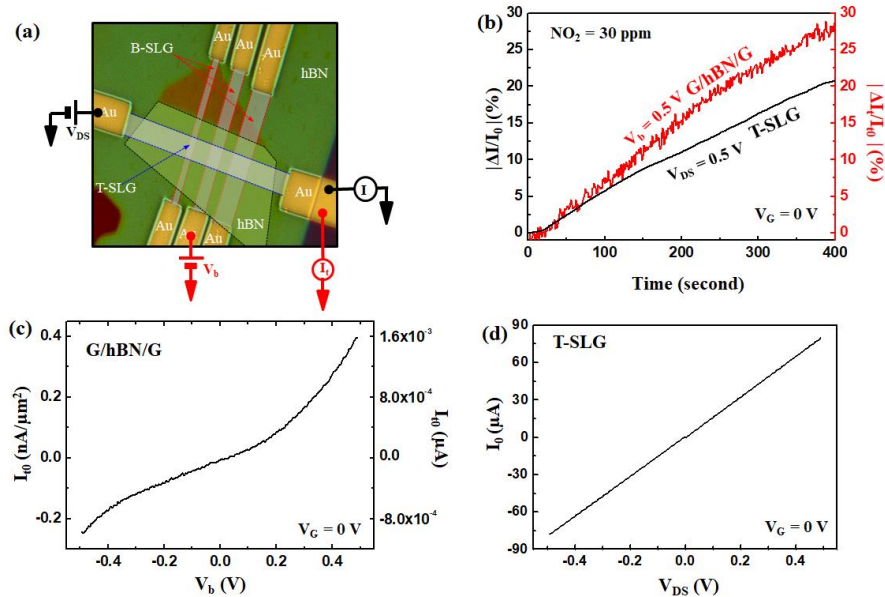


Figure S4. (a) Schematic diagram of the sensing of the concentration of NO₂ gas by a T-SLG FET and a t-G/hBN/G FET. (b) Absolute value of the sensitivity ($|\Delta I/I_0|$) for T-SLG FET ($V_{DS} = 0.5$ V, $V_G = 0$ V) and ($\Delta I_t/I_0$) G/hBN/G FET ($V_b = 0.5$ V, $V_G = 0$ V) under NO₂ gas 30 ppm as a function of time. (c) I_0 vs V_b curve for the t-G/hBN/G FET. Here y-axis show I_0 per unit tunneling area (nA/ μm^2) and raw current value of I_0 (μA). (d) I_0 vs V_b curve for the T-SLG. Here we can confirm that the sensitivity for tunneling FET is large albeit smaller absolute tunneling current than T-SLG.

5. Gas-molecule-sensing sensitivity of a t-GFET under a gas mixture condition

A semiconductor gas sensor detects target molecules by identifying the polarity, during which NO_2 and NH_3 molecules are generally employed as acceptor and donor types of molecules, respectively. In Figs. S5(a) and (b), instances of the significant suppression of $\Delta I_t/I_{t0}$ from 43% to -0.2 % for a t-G/ WS_2 /G FET and from 16.6 % to 6.5 % for a t-G/hBN/G FET were noted when tuning the NO_2 : NH_3 ratio from 40 : 0 to 1 : 40. In Fig. S5(c), the positive and small signal for G/ WS_2 /G FET can be observed under NO_2 : $\text{NH}_3 = 0$: 40. Since the magnitude of $\Delta I_t/I_{t0}$ for NO_2 : $\text{NH}_3 = 0$: 40 is too smaller than other mixed condition, $\Delta I_t/I_{t0}$ for NO_2 : $\text{NH}_3 = 0$: 40 and 40 : 0 were not included in fingerprint map in Fig. 4 and S6. This indicates that the combination of NH_3 molecules and NO_2 molecules influences the adsorption onto the t-GFETs. Such a substantial influence of NH_3 molecules on $\Delta I_t/I_{t0}$ is also examined through calculations of $|\Delta I_t/I_{t0}|$ through a WS_2 barrier as a function of the NO_2 concentration (see Fig. S5(d)). It is clearly seen that the magnitude of $|\Delta I_t/I_{t0}|$ with a given amount of NH_3 gas is significantly reduced compared to that in the NO_2 single-gas case. The calculation results are consistent with the experimental data. Details of the calculation will be introduced and discussed in Sec. 7 of the Supporting Information. By assembling this $\Delta I_t/I_{t0}$ at $t = 360$ s by tuning the NO_2 : NH_3 ratio from 40 : 1 to 1 : 40, we can plot a fingerprint map of $\Delta I_t/I_{t0}$ as a function of the NO_2 and NH_3 concentrations, as shown in Figs. 4 and S6.

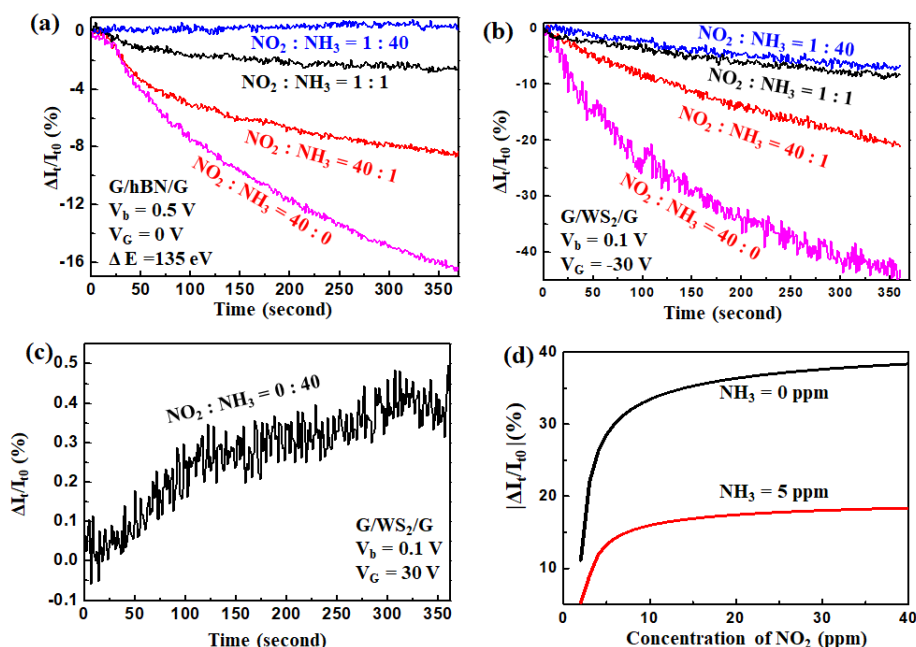


Figure S5. (a), (b) Relative tunneling current variation ($\Delta I_t/I_{t0}$) of (a) t-G/hBN/G and (b) t-G/ WS_2 /G FETs as a function of time under different mixed gas conditions with the following parameters: NO_2 : $\text{NH}_3 = 40$: 0 (pink), 40 : 1 (red), 1 : 1 (black), and 1 : 40 (blue). Here, t-G/hBN in (a) is characterized by a t-GFET with $\Delta E = 135$ meV, as shown in Fig. S3c. (c) $\Delta I_t/I_{t0}$ of t-G/ WS_2 /G FET as a function of time under NO_2 : $\text{NH}_3 = 0$: 40. (d) Absolute value of the relative tunneling current variation, namely the sensitivity ($|\Delta I_t/I_{t0}|$) as a function of the concentration of NO_2 under 0 ppm (black line) and 5 ppm (red line) of NH_3 .

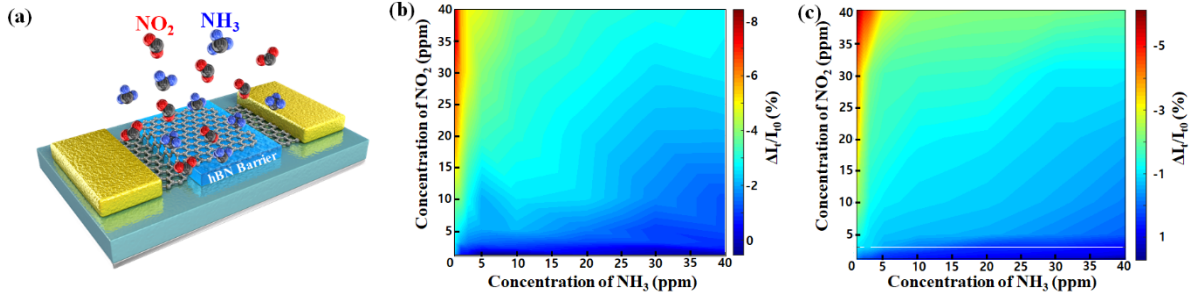


Figure S6. (a) Schematic diagram of the sensing of the concentration ratio between donor (NH_3) and acceptor (NO_2) types of molecules in a mixed gas condition by a tunneling field-effect transistor structured with a t-GFET. (b), (c) Fingerprint mapping of the sensitivity ($\Delta I_t/I_{t0}$) from 6.1 % to -1.7 % corresponding to concentration ratios of $\text{NO}_2 : \text{NH}_3$ from 40 : 1 to 1 : 40 of t-G/hBN/G FETs for (b) $\Delta E \sim 223$ meV and (c) $\Delta E \sim 135$ meV as a function of the concentrations of NO_2 and NH_3 . Since the effective tunnel barrier for off-state of WS_2 is much smaller than that for invariant hBN, the sensitivity by molecule adsorption for G/ WS_2 /G FET in Fig. 4 is higher than for G/hBN/G FET, albeit similar trends of sensitivity variation under gas mixed condition with Fig. 4. Furthermore, because the larger (b) $\Delta E \sim 223$ meV allows us to slightly suppress effective tunnel barrier due to larger bias electric field than (c) $\Delta E \sim 135$ meV, the sensitivity for (b) $\Delta E \sim 223$ meV with molecule adsorption is larger than (c) $\Delta E \sim 135$ meV. Here, the sensitivity maps with $\Delta I_t/I_{t0}$ under exposure to gas conditions were extracted after ~ 360 s from the $\Delta I_t/I_{t0}$ vs time curves with $V_b = 0.1$ V, $V_G = -30$ V.

6. Electrostatic model for t-G/ WS_2 /G FETs

We provide an electrostatic model for the t-G/ WS_2 /G FETs used in the experiments. In this model, the T-SLG and B-SLG are regarded as 2D charged surfaces, of which carrier densities can be controlled by V_G and V_b , and thus, they are given as a function of V_G and V_b . We consider a coupled capacitor model to describe the voltage-dependent carrier densities on both T-SLG and B-SLG with the following series of equations:

$$\begin{aligned}\epsilon_{\text{WS}_2} E_3 &= en_T, \\ \epsilon_{\text{WS}_2} E_3 - \epsilon_{\text{hBN}} E_2 &= en_B, \\ \epsilon_{\text{hBN}} E_2 - \epsilon_{\text{SiO}_2} E_1 &= 0, \\ \epsilon_{\text{SiO}_2} E_1 &= ep, \\ e(n_T + n_B + p) &= 0,\end{aligned}$$

where E_1 , E_2 , and E_3 are electric fields inside SiO_2 , hBN substrates, and a few-layer WS_2 sandwiched by T-SLG and B-SLG, respectively. n_T , n_B , and p are the carrier densities on the T-SLG, B-SLG, and back-gate interface underneath SiO_2 substrate, respectively. ($p < 0$) ϵ_{hBN} , ϵ_{WS_2} and ϵ_{SiO_2} are the relative permittivities of each dielectric material. After some algebra, carrier densities on T-SLG and B-SLG are found as below:

$$\begin{aligned}n_B(V_G, V_b) &= \frac{\epsilon_{\text{hBN}} \epsilon_{\text{SiO}_2}}{2e(L_{\text{hBN}} \epsilon_{\text{SiO}_2} + L_{\text{SiO}_2} \epsilon_{\text{hBN}})} V_G - \frac{2\epsilon_{\text{WS}_2}(L_{\text{hBN}} \epsilon_{\text{SiO}_2} + L_{\text{SiO}_2} \epsilon_{\text{hBN}}) + \epsilon_{\text{hBN}} \epsilon_{\text{SiO}_2} t}{2e(L_{\text{hBN}} \epsilon_{\text{SiO}_2} + L_{\text{SiO}_2} \epsilon_{\text{hBN}}) t} V_b, \\ n_T(V_G, V_b) &= \frac{\epsilon_{\text{hBN}} \epsilon_{\text{SiO}_2}}{2e(L_{\text{hBN}} \epsilon_{\text{SiO}_2} + L_{\text{SiO}_2} \epsilon_{\text{hBN}})} V_G + \frac{2\epsilon_{\text{WS}_2}(L_{\text{hBN}} \epsilon_{\text{SiO}_2} + L_{\text{SiO}_2} \epsilon_{\text{hBN}}) + \epsilon_{\text{hBN}} \epsilon_{\text{SiO}_2} t}{2e(L_{\text{hBN}} \epsilon_{\text{SiO}_2} + L_{\text{SiO}_2} \epsilon_{\text{hBN}}) t} V_b,\end{aligned}$$

where L_{hBN} , L_{SiO_2} and t are the thicknesses of hBN and SiO_2 substrates and the sandwiched WS_2 layer. Here, we do not consider the screening effects which result in a non-linear response of the carrier density to the external voltages, for simplicity. With the obtained charge densities, the chemical potentials (Fermi energies) of T-SLG and B-SLG are given by

$$\mu_B(V_G, V_b) = s \hbar v_F \sqrt{\pi |n_B(V_G, V_b)|},$$

$$\mu_T(V_G, V_b) = s\hbar v_F \sqrt{\pi |n_T(V_G, V_b)|},$$

where $s = \text{sgn}(n)$, is a sign function. In fact, in equilibrium, the Fermi energies of T-SLG and B-SLG should be aligned at the same energy, so band alignment occurs as depicted in Fig. S7(a).

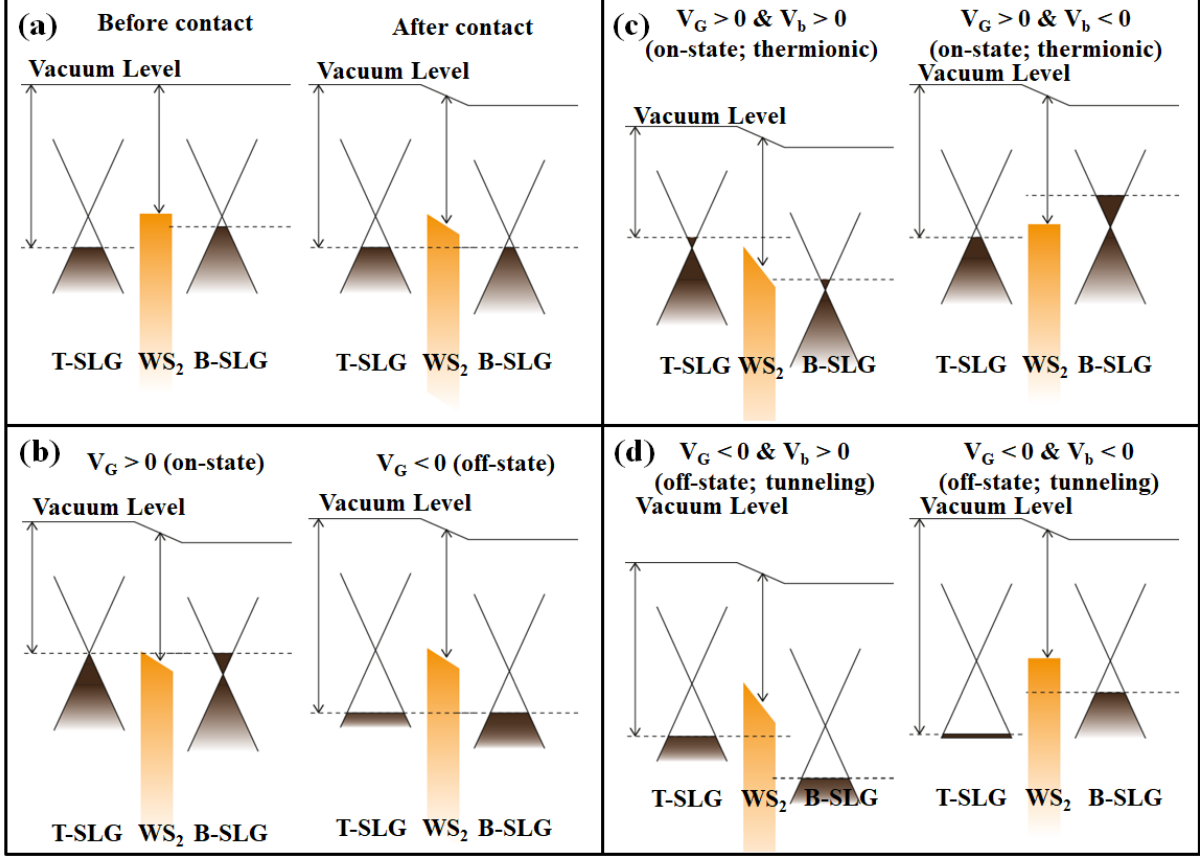


Figure S7. Schematics of the energy diagrams considered in this study. (a) Dirac cones are shifted in the t-G/WS₂/G FETs due to the Fermi energy alignment. The Fermi energy resides close to the conduction band edge of WS₂, so effective potential barrier is low enough to cause Fowler-Nordheim or thermionic transport of thermally excited carriers. (b) After contact, the Fermi energy of the t-G/WS₂/G FETs can be controlled by applying V_G . For $V_G > 0$, the Fermi energy can exceed the WS₂ tunnel barrier, yielding on-state with thermionic transport over the barrier. For $V_G < 0$, on the other hand, the Fermi energy can be lowered down to deeper energy levels, causing off-state with direct tunneling throughout the WS₂ tunnel barrier. (c-d) Schematic diagrams for influence of applying V_b between T-SLG and B-SLG, for on-state and off-states, respectively. Depending on the polarity of applying V_b , the Fermi energy of B-SLG can be either escalated or lowered, resulting in non-zero net tunneling current throughout the t-G/WS₂/G FETs.

First, let us consider the simplest situation, $V_b = 0$, and $V_G \neq 0$. In this case, T-SLG and B-SLG must remain in electrical equilibrium, so it is straightforwardly seen that $n_T = n_B$. Of course, this equilibrium condition satisfies the charge neutrality for whole system, i.e., $n_T + n_B + p = 0$. Figure S7(b) shows schematic diagrams of the t-G/WS₂/G FETs which reside in equilibrium situation. The displayed schematics in Fig. S7, however, exhibit different charge density distributions. This difference originates from the initial doping densities of T-SLG and B-SLG in ambiguous conditions, which will be discussed in the next section.

Next, for $V_b \neq 0$, T-SLG and B-SLG are no longer in equilibrium due to the V_b induced additional charge densities, as aforementioned. One can easily note that the charge neutrality is still satisfied despite finite V_b . If we assume $V_G \gg V_b$, Fermi energies of T-SLG and B-SLG can be expressed by:

$$\begin{aligned}\mu_B(V_g, V_b) &= s\hbar v_F \sqrt{\pi|n_0|} - \frac{\alpha}{2} V_b, \\ \mu_T(V_g, V_b) &= s\hbar v_F \sqrt{\pi|n_0|} + \frac{\alpha}{2} V_b,\end{aligned}$$

where n_0 is a ‘background’ charge density determined by V_G only, and α is a V_G dependent factor. Further, this simplified expression for Fermi energies of T-SLG and B-SLG has been widely accepted as an intuitive way of developing electrostatic models for various t-G/TMDC/G FETs [42, 43, 44, 45]. Therefore, it is obvious to expect simultaneous changes in charge densities on T-SLG and B-SLG as V_b varies, for given V_G . (see Figs. S8(b) and (c)) We can accordingly locate position of the charge neutrality points ($\mu_0 = 0$ meV) of T-SLG and B-SLG, respectively, by finding conditions to make μ_T and μ_B vanish.

7. Initial doping effects on the voltage-dependent tunneling of Dirac fermions in t-G/WS₂/G FETs

As displayed in Figs. 1 and S3, graphene sheets in a FET are initially doped in the absence of applied voltage. At equilibrium, the Fermi energies of T-SLG and B-SLG are identical. Subsequently, there emerges an electric field between the two graphene layers, leading to band tilting inside the WS₂ insulator. The initial doping-induced electric field is expressed as $\Delta E t$, where $\Delta E = \Delta E_{T-SLG} - \Delta E_{B-SLG}$ and t is the thickness of the WS₂ tunnel layer. ΔE_{T-SLG} and ΔE_{B-SLG} were found to be approximately 157 and 55 meV, respectively, according to the I- V_{DS} curves for T-SLG and B-SLG using the following relationship between the charge density and the applied gate voltage,

$$n_{T(B)-SLG}(V_G) = \frac{\epsilon_{hBN} \epsilon_{SiO_2}}{2e(\epsilon_{hBN} L_{SiO_2} + \epsilon_{SiO_2} L_{hBN})} V_G,$$

where ϵ_{hBN} and ϵ_{SiO_2} are the electric permittivities of the h-BN and SiO₂ substrates with thicknesses of L_{hBN} and L_{SiO_2} , respectively. Note that here positive values of the charge density are set for the electron-doped states, and vice versa. Once we find the charge-neutral position in the I- V_{DS} curves, it is straightforward to obtain the initial doping levels with $\mu = \text{sign}(n)\hbar v_F \sqrt{\pi|n|}$, where μ is the chemical potential of graphene. Figure S8(a) shows an energetic diagram of t-G/WS₂/G FETs for $V_G = 0$ V and $V_b = -0.2$ to 0.2 V. Indeed, the WS₂ tunnel barrier is tilted by as much as ΔE , and each graphene layer is shifted to either a higher or lower energy level owing to the initial doping level. While the initial doping-induced electric field between T-SLG and B-SLG are in equilibrium in the absence of V_b resulting in no net tunneling current throughout the structures, under applying V_b on B-SLG with grounded T-SLG, Fermi energy of T-SLG is escalated by inducing the number of electrons. On the other hand, Fermi energy of B-SLG is lowered because the same number of electrons as the induced charge on B-SLG are migrated to T-SLG via V_b . In the presence of V_b , therefore, T-SLG and B-SLG are no longer in equilibrium, resulting in non-zero net tunneling current. Here, the escalation of T-SLG Fermi energy implies the variable reference point of electric potential through which V_b are measured. As V_b decreases, the Dirac cone of T-SLG is lowered, whereas the Dirac cone of B-SLG is increased, resulting in a flat WS₂ tunnel barrier when $V_b = -0.1$ V. In this case, the chemical potential of B-SLG is at the conduction band edge of WS₂, allowing thermionic transport to begin to contribute to the tunneling current via thermal fluctuation. For $V_b < -0.1$ V, the tunneling current continues to increase as a function of V_b because the number of tunneling carriers increases via both thermionic transport and Fowler-Nordheim tunneling processes depending on their energy levels. On the other hand, when $V_b > 0$, the Dirac cone of T-SLG is shifted to a higher energy and the Dirac cone of B-SLG is lowered by as much as $eV_b/2$. In this case, it is clearly observable that the behavior of the tunneling current increases as a function of V_b , as Fowler-Nordheim tunneling becomes dominant where the effective thickness of the tunnel barrier is thinner than in the direct tunneling regime. As expected, greater tunneling current is achieved as V_b increases further. Next, when $V_G = 30$ V is applied, the Fermi energies in both T-SLG and B-SLG are escalated. Consequently, T-SLG is nearly undoped and B-SLG becomes electron-doped (see the middle diagram in Fig. S8(b)). Owing to the V_G -induced Fermi energy escalation, the system is in an on-state, where thermionic transport plays a dominant role in the tunneling process. Indeed, the chemical potentials in either T-SLG or B-SLG are

at much higher energy levels than the WS_2 tunnel barrier height, leading to the nearly linear I_t - V_b curve depicted in Fig. 2(d). Contrary to the on-state, when $V_b = -30$ V is applied, the Fermi energies of T-SLG and B-SLG become lower, as exhibited in Fig. S8(c). Thus, the system is in an off-state, where direct tunneling mainly contributes to the tunneling current. For a small V_b , the system still resides in the off-state regardless of the V_b polarity. However, the tunneling current exhibits somewhat different behavior for relatively large values of V_b . For example, for $V_b = -0.2$ V, the chemical potential of B-SLG is increased and the effective barrier height becomes quite small such that one can expect a large amount of tunneling current through the tunnel barrier. Similarly, for $V_b = 0.2$ V, the Fowler-Nordheim tunneling partly contributes to the tunneling current as a consequence of the escalation of the T-SLG chemical potential.

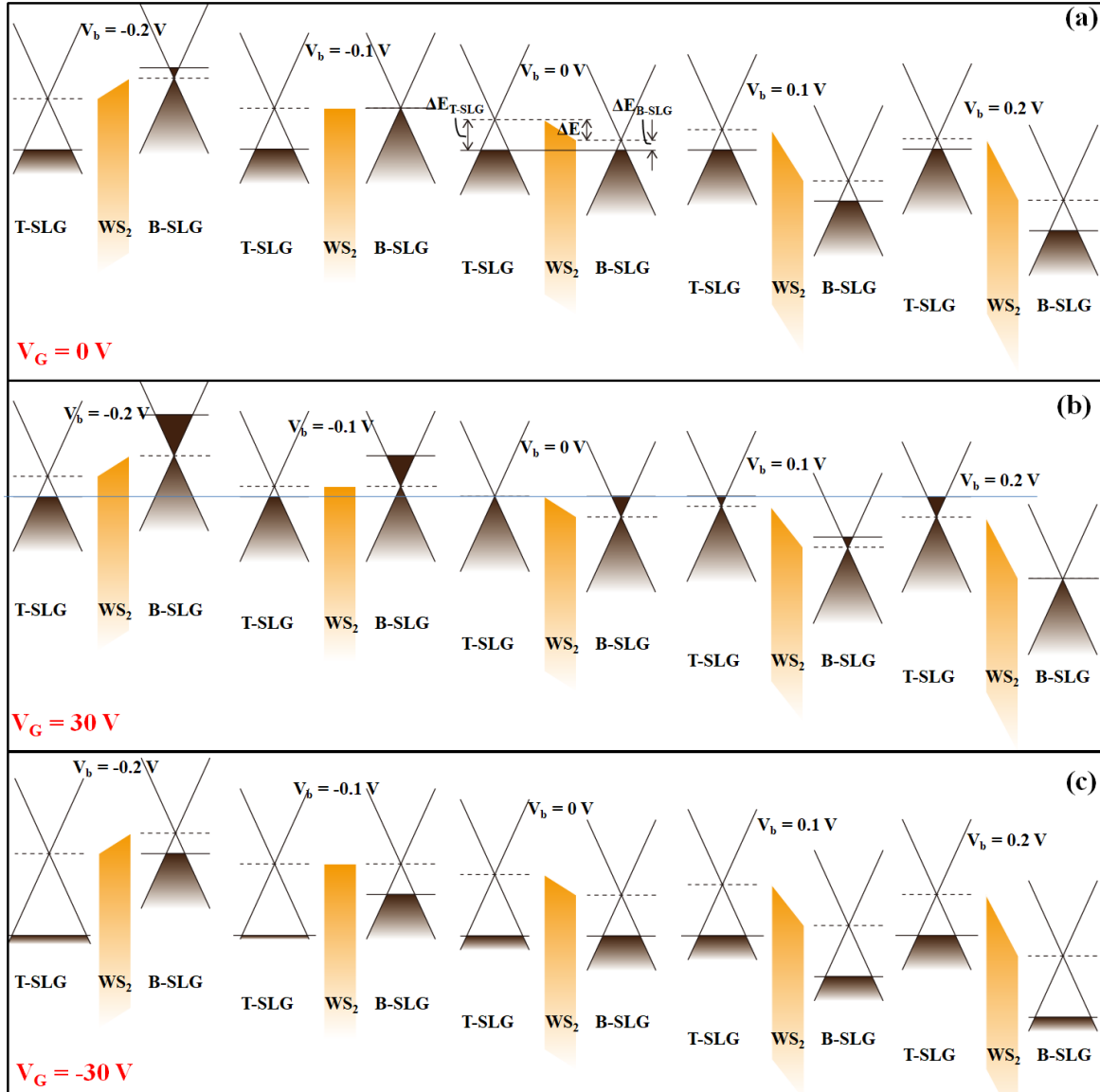


Figure S8. (a)-(c) Schematics of the energetic diagrams for $V_G =$ (a) 0, (b) 30, and (c) -30 V. Each panel contains a series of diagrams for V_b sweeps from -0.2 to 0.2 V. Solid and dashed lines indicate the chemical potentials and the charge-neutral positions in each graphene layer, respectively. $\Delta E_{\text{T(B)-SLG}}$ indicates the doping level of each graphene layer, and ΔE indicates the difference as reflected in the band tinting of the WS_2 tunnel layer. Because T-SLG and B-SLG are separated by an atomically thin WS_2 layer, a fairly large electric field can be produced between T-SLG and B-SLG due to the small value of V_b . Such a large electric field accordingly induces a large number of carriers on B-SLG, leading to a substantial shift of the Dirac cone. As a result, the band diagrams of B-SLG are significantly changed by the small V_b values.

8. Formalism for the calculation of the tunneling current through t-G/WS₂/G FETs

In this study, we undertook calculations of the tunneling current density in graphene vertical heterostructures using the following equation [44, 45]:

$$j(V_G, V_b, T) = \frac{4\pi e}{\hbar} \int_{-\infty}^{+\infty} D_{T\text{-SLG}}(E, V_b) D_{B\text{-SLG}}(E, V_b) \tau(E, V_b) [f_{B\text{-SLG}}(E, V_G, V_b, T) - f_{T\text{-SLG}}(E, V_G, V_b, T)] dE,$$

where

$$D_{T(B)\text{-SLG}}(E, V_b) = \frac{g_s g_v |E \pm V_b/2|}{2\pi \hbar^2 v_F^2}$$

denotes the densities of the states of T-SLG and B-SLG with spin and valley degeneracies of $g_s = g_v = 2$, respectively, and where

$$f_{T(B)\text{-SLG}}(E, V_G, V_b, T) = \frac{1}{1 + e^{(E - \mu_{T(B)\text{-SLG}})/k_B T}}$$

are the Fermi-Dirac distributions in T-SLG and B-SLG with the chemical potentials of $\mu_{T(B)\text{-SLG}}$, and

$$\tau(E, V_b) = \Gamma^2 e^{-2\sqrt{\frac{2m_{WS_2}^*}{\hbar}} \int_{-t/2}^{t/2} k_z(E, V_b, z) dz}$$

is the transmission probability through the WS₂ layer with an effective mass of WS₂ $m_{WS_2}^*$ and with the WS₂ thickness t . Here, it is important to comment on the energy-independent prefactor Γ in units of $eV\text{\AA}$, which implies how the tunneling charge carriers are dissipated via inelastic scattering³; i.e., the smaller the value of Γ , the more reduced τ becomes. We assume that the transmission of charged carriers from T-SLG to B-SLG is perfect, leading to $\tau = 1$ in the thermionic transport regime.

For the tunneling current formula, the effects of gas-molecule-induced doping in T-SLG are taken into account via the change in the chemical potential, stemming from the variation of the carrier density. The saturation feature of $\Delta I/I_0$ is well described by $\Delta n(t) = n_s (1 - e^{-\gamma_{ad} t})$ with the saturated density n_s and the adhesion rate of the gas molecules γ_{ad} onto T-SLG. Furthermore, γ_{ad} should be given as a function of the gas concentration C ; i.e., $\gamma_{ad}(C) = \gamma_0 + \gamma_1 \ln(C + \alpha)$, where the parameters $\gamma_{0,1}$ and α are found by fitting to the experimental data in Fig. 3(c). The implication of n_s and γ_{ad} is as follows: γ_{ad} indicates how a gas molecule is adsorbed onto T-SLG, and n_s tells us how an adhered molecule donates or accepts a charge carrier to or from the T-SLG. In addition, for mixed gas conditions, we are also able to use the same calculation to find the parameters for NO₂ and NH₃ gas molecules in the mixed gas. It is important to note that n_s and γ_{ad} for each molecule in the mixture gas are somewhat different from those in the single-gas condition. In this argument, we started with the single gas of NH₃ molecules and observed how the parameters n_s and γ_{ad} for NO₂ molecules change when inserting NH₃ molecules with the given n_s for NH₃. Thus, the doping contribution of an individual NH₃ gas molecule is considered here as a constant correction. Based on the proposed calculation model, although the detailed mechanisms of the gas mixture, such as inter-molecular reactions, cannot be fully interpreted, we can deduce here how the chemical reaction is changed by the gas-molecule-induced doping effect in T-SLG in the mixed gas condition by determining n_s and γ_{ad} via fitting. Table I lists the parameters utilized after fitting the calculated results to the experimental data for various voltages in either single or mixed gas conditions. Under exposure to NO₂ as a single gas, γ_{ad} for $V_b = -0.1$ V tends to be greater than that for $V_b = 0.1$ V, indicating that the potential for adsorption onto T-SLG changes according to the polarity of V_b . Moreover, the doping effect of the NO₂ molecule in the single-gas condition varies depending on the voltage configuration. This voltage-dependent doping effect may be associated with the polarity of the applied V_b , showing a tendency to increase for $V_b < 0$. Next, in mixed-gas cases, n_s and γ_{ad} are determined for various concentration ratios. The charging effect from an adhered NH₃ molecule is found to be unchanged by different ratios of the gas mixture, and this appears to be consistent with the contention of the weak contribution of NH₃ molecules in the gas mixture, as shown in Fig. 4 in the main text. In the same context, the γ_{ad} values of NH₃ gas molecules are also mostly unchanged for different concentration ratios. In contrast, the γ_{ad} values of

NO₂ gas molecules exhibit dependence on the concentration ratio. In consequence, we can infer that the chemical reaction of an NO₂ molecule is relatively sensitive to the presence of other species of molecules.

Table I. The saturated charge density and the adhesion rate for gas-molecule-induced doping effects in t-G/WS₂/G FETs for various cases. The adhesion rates apply to specific concentrations of gases. Here, the red values represent n_s and γ_{ad} in the mixed condition.

V _G (V)	V _b (V)	n_{s,NO_2} (10 ¹² cm ⁻²)	n_{s,NH_3} (10 ¹² cm ⁻²)	C _{NO2} (ppm)	C _{NH3} (ppm)	γ_{ad,NO_2} (mHz)	γ_{ad,NH_3} (mHz)
-30	-0.1	-2.07	-	30	0	4.82159	-
-30	+0.1	-0.621	-	30	0	2.55598	-
-30	+0.1	-0.39125	0.436563	20	20	7.3137	3.31199
-30	+0.1	-0.39125	0.436563	40	20	7.3137	3.08073
-30	+0.1	-0.436563	0.436563	20	40	5.68844	3.31199
-30	+0.1	-0.436563	0.436563	40	40	5.68844	3.08073
+30	-0.1	-1.403	-	30	0	4.82159	-
+30	+0.1	-0.667	-	30	0	2.5764	-

References

42. L. Britnell et al., Science, 2013, 340, 1311-1314.
43. T. Georgiou et al., Nat. Nanotechnol., 2013, 8, 100.
44. N. Myoung, K. Seo, S. J. Lee and G. Ihm, ACS Nano, 2013, 7, 7021.
45. E. R. Rodriguez-Nieva, M. S. Dresselhaus and L. S. Levitov, Nano Lett., 2015, 15, 1451.